Computational Materials Science 191 (2021) 110344

Contents lists available at ScienceDirect

Computational Materials Science

journal homepage: www.elsevier.com/locate/commatsci

Evolution of high-pressure metastable phase Si-XIII during silicon nanoindentation: A molecular dynamics study

Lin Zhang *, Jiwang Yan

Department of Mechanical Engineering, Keio University, Yokohama 223-8522, Japan

ARTICLE INFO

Keywords:
High-pressure Si-XIII phase
Berkovich indenter
Evolution
Crystalline surface
Molecular dynamics

ABSTRACT

Berkovich indenters are widely employed in nanoindentation experiments of single-crystal silicon, in molecular dynamic simulations of silicon nanoindentation, however, spherical indenters are generally employed. To close this gap, in this paper, a series of molecular dynamic simulations are conducted on (001), (101), and (111) silicon surfaces to explore the evolution of high-pressure phases. Several possible silicon phases are tracked by coordination number (CN), radial distribution function (RDF), and angular distribution function (ADF). Results show that the metastable phases and the high-pressure phases present different symmetrical patterns along different crystallographic orientations. A large amount of high-pressure phase Si-XIII, which is seldomly observed in nanoindentation using a spherical indenter, is first discovered under the Berkovich indenter, and the evolution mechanism is characterized by tracking the position transition of labeled silicon atoms. As a transition phase for high-pressure phase Si-II and Si-XIII, bct5 phase is found in the {111} [110] slip systems, which is related with slipping flatten lattice structures. Different from the phase transformation criterion for Si-II, the transformation from Si-I to Si-XIII companies with the local elastic deformation of (001) surface. The atoms in the three neighboring unit cells are compressed into a uniform long-distance ordered crystal structure. Upon indenter extraction and rapid stress releasing, the elastic deformation of the crystal surface resumes incompletely. A part of Si-XIII recovers to pristine Si-I and the rest changes into amorphous phase. The distribution of local hydrostatic pressure and von Mises stress in the phase transformation regions indicates that the concentrated hydrostatic pressure and specific stress induce this high-pressure silicon phase. This research clarifies the evolutionary process of Si-XIII phase generation and enriches fundamental understanding on the mechanisms of silicon phase transformations in nanoindentation.

1. Introduction

As a critical material in micro/nanoelectro-mechanical system (MEMS/NEMS) and integrated circuit (IC), monocrystalline silicon is investigated intensively in the past few decades in order to deeply understand its mechanical behavior at micro/nanoscale [1]. A great deal of efforts has been made in revealing its deformation mechanism at micro/nanoscale, such as phase transformations under high pressure loading and subsequent pressure release [2,3]. It has been generally accepted that phase transformation of monocrystalline silicon is a major mechanism of deformation at microscale, which dramatically changes its mechanical [4], chemical [5], and electrical performances [6,7]. Diamond anvil cell (DAC) [8,9] and nanoindentation [2,3,6,7,10–12] are two commonly accepted approaches to investigate the phase transformations in monocrystalline silicon under a contact load. Due to its high measurement resolution and good compatibility of samples, nanoindentation has been obtained increasing attentions [13–16].

Through experimental analysis and characterization [2,3,6,10–12,15] as well as numerical simulations on micro/nanoscales [17–20], some phase transformations in monocrystalline silicon during nanoindentation have been clarified. It is commonly accepted that in the loading process, the pristine diamond cubic Si-I phase, with lattice parameter $a = 5.4321$ Å, undergoes the first phase transformation into a metallic Si-II (β-Si) phase at a pressure of $10 \sim 12$ GPa, which is a dense body-centered tetragonal b-tin structure with lattice parameter $a =$ 4.684 Å and $c = 2.585$ Å. This transformation companies with about 22% volume shrinkage, leading to discontinuities (pop-ins) in the *P-h* curve. With higher pressure, other five high-pressure silicon phases, i.e. Si-XI, Si-V, Si-VI, Si-VII, and Si-X phases, appears. In the unloading process, the high-pressure phases fail to recover to the Si-I phase. The

* Corresponding author.
E-mail address: zhanglin@keio.jp (L. Zhang).

https://doi.org/10.1016/j.commatsci.2021.110344
Received 1 November 2020; Received in revised form 24 January 2021; Accepted 27 January 2021
Available online 8 February 2021

phase transformation is highly dependent on the indentation load and pressure release rate [15]. Generally, a high indentation load and a low-pressure release rate will promote the appearance of a mixture of Si-XII (rhombohedra structure, or R8) and Si-III (body-centered-cubic structure, or bc8) phases. On the contrary, a low indentation load and a high pressure release rate, the Si-II phase trends to transform into amorphous silicon (α-Si) [3,15].

Although many studies on phase transformation of monocrystalline silicon have been reported, the understanding on the phase transformation is still far from complete. In contrast to DAC, nanoindentation induces not only hydrostatic pressure but high shear stress as well, which has been reported to promote Si-I to Si-II phase transformation at a lower pressure (8.5 GPa) and causes more complicated phase transformation [21]. In spite of the rapid development of characterization techniques, real-time *in situ* characterization of the structural transformation taking place beneath the surface during nanoindentation is still difficult due to the extremely small dimension [19,20,22]. On the other hand, large-scale molecular dynamics (MD) simulation can provide detailed information about interior phenomena. With the aid of MD, some studies reported phase transformation beneath a semi-spherical indenter and the elastoplastic behavior of silicon. For example, Cheong and Zhang indicated the change from Si-I to Si-II (β-Si) under hydrostatic pressure by flattening of the tetrahedron structure in diamond cubic silicon [23]. Kim and Oh identified metastable phases with fourfold coordination, namely Si-III and Si-XII, in the slip direction of monocrystalline silicon transformed by inhomogeneous distortion [24]. Sun *et al.* investigated the orientation-dependent mechanical behavior and the corresponding phase transformation of monocrystalline silicon [25]. Mylvaganam *et al.* investigated the phase transformation of monocrystalline silicon by both MD simulation and in situ scanning spreading resistance microscopy (SSRM) analyses [26].

In spite of the aforementioned intensive research, there is few studies adopting Berkovich indenter in MD simulations. However, it is the most used indenter in experiments. The shape of indenter is a main factor affecting the evolution of silicon phases in nanoindentation because of the different distribution of internal stresses. This may help understand the generation mechanism of different new phases, which has not yet been clarified. For example, compared with the high-pressure silicon phase Si-II, which is frequently reported, the occurrence of Si-XIII in nanoindentation is first reported by Mylvaganam *et al.* [26] and seldomly investigated since then. The evolution for phase transformation from Si-I to Si-XIII is still a confusing issue and the occurrence on different crystallographic silicon surfaces is lack of understanding. A possible reason might be that with the spherical indenter, the volume of high-pressure Si-XIII phase is inappreciable, mingling with other silicon phases, which is the most likely to be neglected. On the other hand, different from the Si-II phase transformation, no direct or indirect residual phase transformations after pressure releasing are found in the experiments. Up to now, the occurrence of Si-XIII phase in nanoindentation is confusing.

Facing these issues, this study aims to explore the mechanism of phase transformation of monocrystalline silicon with Berkvioch indenter during nanoindentation at the atomic level. Large-scale MD simulations are carried out to analyze the nanoindentations on the (001), (101), and (111) oriented silicon surfaces. Several possible silicon phases are classified by coordination number (CN), radial distribution function (RDF), and angular distribution function (ADF). The phase transformation process, especially the phase transformation from Si-I to Si-XIII, and the corresponding extension patterns on different crystalline surfaces are carefully investigated. Furthermore, the detailed label tracking strategy is employed to monitor the transition of silicon atoms under pressure. With the aid of local hydrostatic pressure and Von mises stress analysis, the distribution and structure evolution from Si-I to Si-XIII are systemically analyzed.

2. Methods

Large-scale three-dimensional (3D) molecular dynamics simulations are conducted to investigate the transformation of monocrystalline silicon on the (001), (101), and (111) oriented surfaces, as shown in Fig. 1. A standard Berkovich diamond indenter is adopted. Compared with the spherical indenter, Berkovich indenter will induce different stress status in monocrystalline silicon. Because of the large difference on hardness, the diamond indenter, carved out of a (001) oriented diamond, is regarded as a rigid body in the simulation. In order to reduce the boundary effect and size effect, the volume of the silicon specimen should be large. As a result, the simulation becomes computationally expensive. To avoid these problems, the periodic boundary condition is set along the X and Y directions. The specimen surface X-Y plane is indented, which is set as a free surface. The size of the specimen is $60a \times 60a \times 26a$ along the X, Y, and Z directions, consisting of 701,340 atoms, 706,765 atoms and 693,448 atoms for (001), (101), and (111) orientated specimens, where a is the lattice constant of silicon ($a = 0.5431$ nm). The specimen is further divided into three different sections, namely boundary zone, thermostat zone, and Newtonian zone. The bottom layer with a thickness of 10 Å belongs to the boundary zone, which is employed to fix the specimen in the simulation and maintain the proper symmetry of the lattice. Adjacent to the boundary zone is the thermostat zone, which dissipates excessive energy out of the system to keep a constant temperature in NVT ensemble. The rest of the specimen is the Newtonian zone. The motivation of the atoms inside this zone is based on Newton motion equation.

The selection of potential functions affect the accuracy and credibility of numerical simulation [27,28]. In this simulation, Tersoff potential function is employed to describe the interactions between silicon atoms [29]. It has been extensively used in molecular dynamics simulations to predict phase transformation. The cohesive energies for the different phases closely match the experiments in reality. For the interactions between silicon atoms and carbon atoms, Morse potential function is adopted as the previous researches [18]. The indentation speed is set as a constant value for loading and unloading (50 m/s) and the position/velocity update strategy is based on Verlet integration algorithm with a time step of 1.0 fs. The simulation is conducted with the aid of LAMMPS molecular dynamics simulation code, and the Open Visualization Tool (OVITO) and Visual Molecular Dynamics (VMD) are utilized as a tool to view and analyze the results of molecular dynamics simulations [30–32].

In the simulation, several high-pressure silicon phases are identified, namely Si-I, Si-II, Si-III, Si-XII, and bct5. Among possible characterization approaches, it is now generally accepted that the techniques of coordination number (CN), radial distribution function (RDF) and angular distribution function (ADF) are capable to identify different

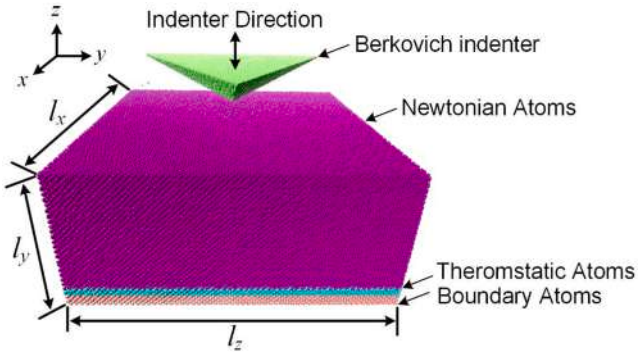

Fig. 1. Schematic diagram of 3D molecular dynamics model of monocrystalline silicon for nanoindentation with Berkovich indenter. The size of the silicon specimen is set $l_x \times l_y \times l_z = 32.586$ nm $\times$ 32.586 nm $\times$ 14.121 nm. In the simulation, the velocity of the abrasive is $v = 50$ m/s^{-1} along z direction.

phases in the simulation. Si-I has four nearest neighbors at a distance of 2.35 Å at ambient pressure, while the Si-II has six nearest neighbors, four at a distance of 2.42 Å and two at a distance of 2.57 Å at a pressure of 10.3 GPa. Accompanied with Si-II metastable phase, bct5 is identified with 5 nearest neighbors, one at a distance of 2.31 Å and four at a distance of 2.44 Å. These phases can be classified by different coordination number within the near range. During the retraction process, several metastable structure phase transformations are discovered, i.e. Si-III and Si-XII phases. As the diamond cubic phase Si-I and two metallic phase Si-III and Si-XII have the same coordinate number, it is impossible to distinguish them by CN directly. As for the surrounding topological structures, while different, it's the number of non-bonded atoms between 2.6 Å and 3.5 Å. Si-I has twelve non-bonded second neighbors at 3.83 Å, while Si-III has only one non-bonded neighbor at 3.41 Å, and Si-XII has a similar non-bonded neighbor at 3.23 Å or 3.36 Å at 2.0 GPa [8,9,33]. Hence, a larger surrounding environment of each atom is applied to classify different phases with the same CN. This phase classification method has been successfully used to distinguish different phase structures in the course of nanoindentation [24]. Furthermore, RDF is a commonly used approach to classify the different phases in molecular dynamics simulations. However, when coming to a mixture with different phases in small dimensions, the statistical data is not reliable and stable. Hence, in this experiment, the RDF and ADF are used to verify and characterize the detailed phase structures within the congregating region with the same CN.

3. Results

3.1. High-pressure silicon phase distribution

In the simulation, the indentations on the silicon (100), (101) and (111) oriented surfaces to the maximum depth (5.0 nm) result in the maximum load 2.608 μN, 2.676 μN, and 2.917 μN. Fig. 2 is the side cross-section views, which show the distribution of the high-pressure phases due to nanoindentation on the (001) oriented surface at the maximum indentation depth. The atoms in cubic diamond structure with fourfold coordination have been deliberately eliminated in the visualization so that we can clearly see any changes to the crystalline order of the monocrystalline silicon. The rest of the atoms in Fig. 2 only involve boundary atoms and defect-related atoms. In the case of nanoindentation on (001) oriented surface, the silicon atoms with sixfold coordination on (001) oriented surface is concentrated at the center of the deformed region, surrounded by five-coordinated silicon atoms. Several layers of silicon atoms directly beneath the indenter have been fully transformed into amorphous phase. In addition, large areas of high-pressure six-coordinated silicon atoms are congregated beneath the indenter plane. It is evident that the silicon atoms with sixfold coordination beneath the indenter on the (001) oriented surface are completely different in region A* and B*, which are both surrounded by five-coordinated silicon atoms.

Lots of metastable phase atoms near the periphery of the phase transformation region are identified. They are classified as a mixture of Si-III/Si-XII atoms with four nearest neighbors with the distance of 2.8 Å and one non-bonded atom within the distance of 3.5 Å. This metastable silicon phase atoms have also been discovered and reported in previous studies by Du [17] and Kim [24]. In their work, the metastable silicon phases appear in loading and recovers to pristine cubic diamond Si-I after unloading. However, they have never been reported in the experiments. Based on the experimental result, the Si-III and Si-XII phases generally come from the phase transformation from Si-II and are retained during unloading. In order to make clear of the metastable phases, RDF and ADF are employed to obtain more characteristics of the metastable phases, as shown in Fig. 3. For comparison, the corresponding characteristics of cubic diamond phase, Si-III and Si-XII are also labelled with colored dashed lines. For the RDF, two sharp peaks between the 2.0 Å to 4.0 Å are observed. The center values for these peaks are located at 2.35 Å and 3.85 Å. A small RDF peak between the 2.8 Å to 3.5 Å is found for the metastable phase atoms, which is responsible for the identified Si-III/Si-XII phase, as shown in Fig. 3(a). In contrast to one single sharp peak at 109° for the diamond cubic silicon Si-I, a major peak at 111° and a small peak at 90° are noted in the ADF for the metastable phases, which is different from the bond angle of 118° and 99° for Si-III phase and 137° for Si-XII phase [8,9]. Based on the above statement, the phase that was previously considered as Si-III/Si-XII phase should be the distorted diamond cubic structure (DDS) silicon.

Figs. 4 and 5 illustrate cross-section views of the phase transformation for the (101) and (111) oriented surface. Comparing with the case on (001) oriented surface, the types and distributions of the high-

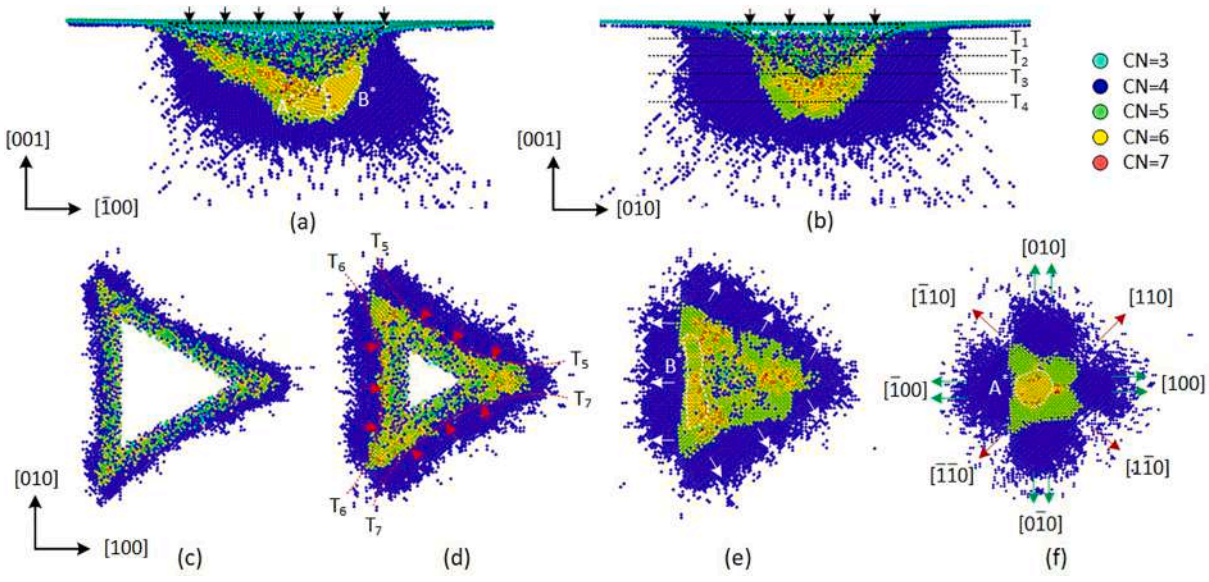

Fig. 2. Side cross-section view and top cross-section view of the phase transformed region induced by nanoindentation on the Si (001) oriented surface. Silicon atoms in diamond cubic structure (Si-I) are invisible. Different coordinated atoms are colored according to the modified coordination number. (a) cross-section view on (010) plane, passing through the tip of the diamond indenter; (b) cross-section view on (100) plane, cross-section view of transformed regions at different depths from the indentation surface (c) 2.0 nm, (d) 3.0 nm, (e) 4.0 nm, and (f) 6.0 nm.

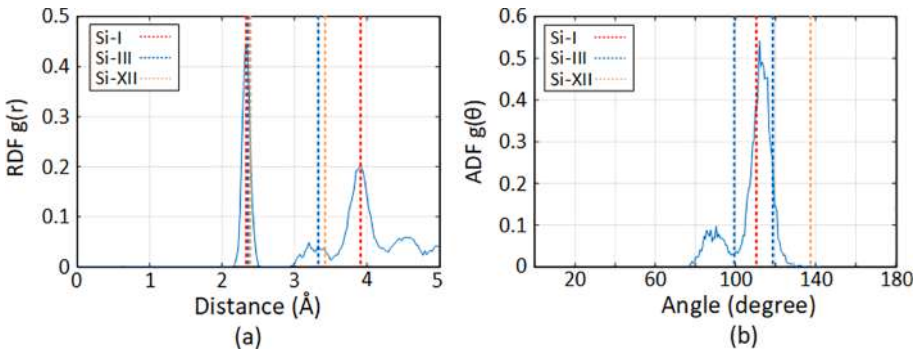

Fig. 3. RDF and ADF of the four-coordinated metastable phases in nanoindentation.

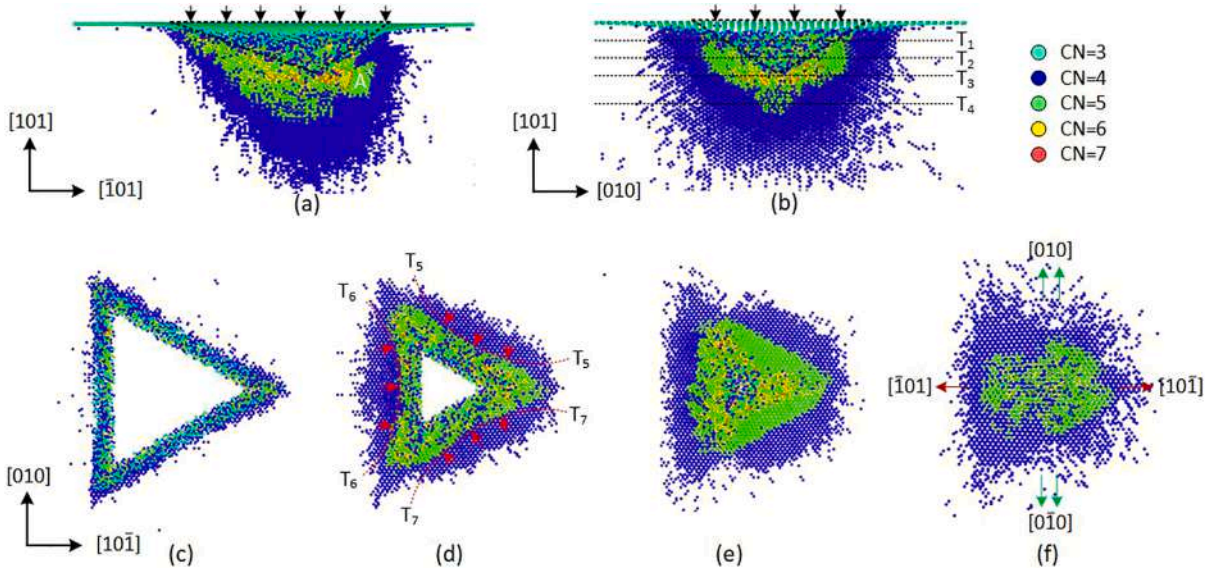

Fig. 4. Side cross-section view and top cross-section view of the phase transformed region induced by nanoindentation on the Si (1 0 1) oriented surface. Silicon atoms in diamond cubic structure (Si-I) are invisible. Different coordinated atoms are colored according to the modified coordination number. (a) cross-section view on (0 1 0) plane, passing through the tip of the diamond indenter; (b) cross-section view on (1 0 1) plane, cross-section view of transformed regions at different depths from the indentation surface (c) 2.0 nm, (d) 3.0 nm, (e) 4.0 nm, and (f) 6.0 nm.

pressure phases under the indenter are quite different depending on the crystallographic orientation. For the (1 0 1) and (1 1 1) oriented surfaces, large number of amorphous silicon atoms are found distributed beneath the indenter over the large pressure-induced area. As illustrated in Figs. 4 and 5, these amorphous silicon atoms are majorly consisted with three, four and five coordinated atoms. Especially, for the (1 0 1) oriented surface, compared with bct5 (five coordinated silicon atoms with crystalline structure) phase, the crystalline structure of Si-II (six coordinated silicon atoms with crystalline structure) is relatively low. The amount of bct5 silicon atoms is several times than that of Si-II phase atoms. For the (1 1 1) oriented surface, much smaller amount of Si-II phase atoms is discovered beneath the indenter. Most of the phase transformed region is filled with bct5 and amorphous atoms.

Furthermore, these high-pressure silicon phases form different symmetrical and anisotropic patterns on the indented surface under the maximum depth. Within the maximum depth, the contours of the high-pressure silicon atoms present similar shapes as the contact edges, while at deeper cross-section view, free from the restraints of the indenter, the high-pressure phases form symmetrical patterns. For instance, on the (0 0 1) oriented surface, the bct5 phase extends along the [1 1 0] and [1 $\bar{1}$ 0] directions, and DDS phase along the [1 0 0] and [0 0 1] directions. While, for the (1 1 0) oriented surface, the bct5 and DDS patterns are different from those on (0 0 1) oriented surfaces. The bct5 phase extends along the [1 $\bar{1}$ 0] direction, and DDS phase along the [1 0 0] direction. For the (1 1 1) oriented surface, the distributions for the high-pressure silicon phases show threefold symmetrical patterns. The bct5 phase is along the [1 1 $-$2], [1 $-$2 1] and [$-$2 1 1] directions, and DDS phase along the [$-$1 $-$1 2], [$-$1 2 $-$1], and [2 $-$1 $-$1] directions.

Although the high-pressure phases present different patterns on different crystallographic surfaces, it is noted that the distributions of the bct5 on any indentation surfaces are consistent with the {1 1 1} [1 1 0] slip systems. The result is similar to previous simulations and experiments [17,24,25]. The consistence is generally accepted as the formation of bct5 phase, which is accomplished by flatting the initially stepped sixfold rings of the diamond lattice and subsequent slipping of flatted planes [34]. The formation of bct5 in nanoindentation is closely related with the high shear stress. Different with the patterns of bct5 on the corresponding crystallographic surfaces, the distribution of DDS is extended along [1 0 0] direction system, in which direction the elastic deformation is most likely to be occurred. It would not be difficult to understand the lowest possibility of plastic deformation on (0 0 1) oriented surface than that for the (1 0 1) and (1 1 1) oriented surface, if the stress conditions, slipping systems and phase transformation are taken into consideration. With the same external load, the resolved shear stress on {1 1 1} planes on the (1 0 0) oriented surface is the smallest among them, on which the DDS phase is able to recover to the pristine diamond structure. The deviatoric stress promotes the phase transformation and decreases the threshold load for the plastic deformation on (1 0 1) and

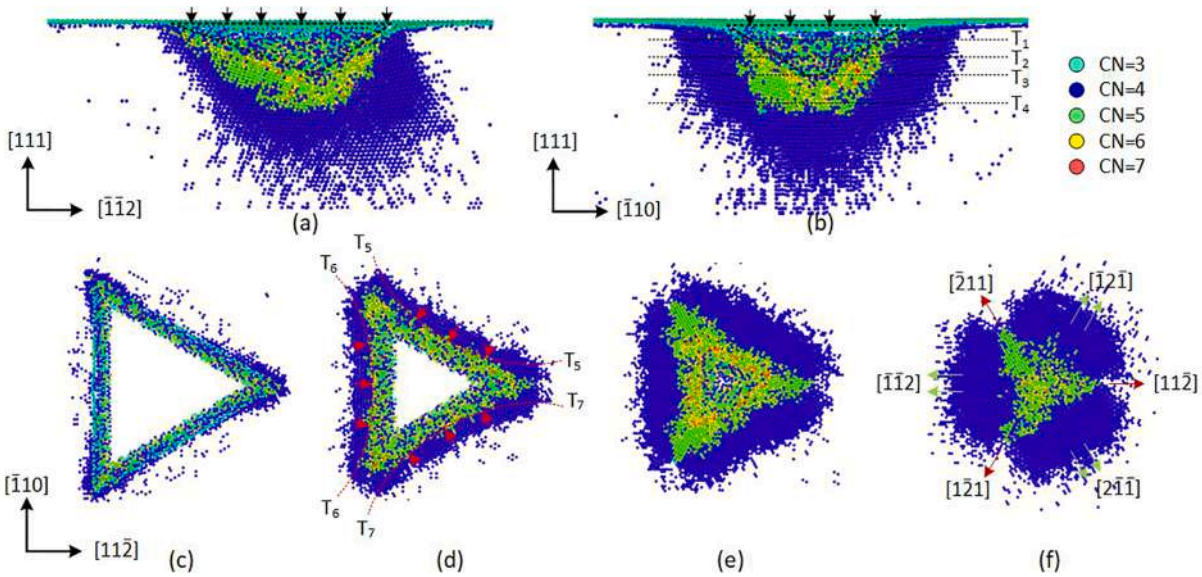

Fig. 5. Side cross-section view and top cross-section view of the phase transformed region induced by nanoindentation on the Si (1 1 1) oriented surface. Silicon atoms in diamond cubic structure (Si-I) are invisible. Different coordinated atoms are colored according to the modified coordination number. (a) cross-section view on (0 1 0) plane, passing through the tip of the diamond indenter; (b) cross-section view on (1 0 0) plane, cross-section view of transformed regions at different depths from the indentation surface (c) 2.0 nm, (d) 3.0 nm, (e) 4.0 nm, and (f) 6.0 nm.

(1 1 1) oriented surfaces.

In order to clearly understand the crystalline structure of the six-coordinated silicon atoms on Si (0 0 1) oriented surface, RDF and ADF of these single-coordinated atoms are illustrated in Fig. 6. For comparison RDF peaks, the characteristics, including bond length and bond angle, of Si-II phase calculated by Tersoff potential [35] are also shown in Fig. 6. Although the RDF peaks have slightly shifted, which are attributed to the severe deformation of the silicon phase, the simulated peaks show great agreement with the previous studies in region A*. The RDF and ADF confirm the formation of Si-II phase in region A*. However, the crystalline structure shows different characteristics of six-coordinated silicon atoms in region B* with Si-II phase in region A*. In contract with several sharp peaks of Si-II phase on ADF, two major peaks at 87° and 135° are examined in ADF, which completely disagrees with the characteristics of Si-II phase. In addition, the detailed atomic structures are also obtained from the simulation model as illustrated in Fig. 7, as well as one single unit cell with bond details. It is clearly seen that the crystalline structure in region B* is totally different from that in region A* (Si-II). These atoms with sixfold coordination in region B* also show great crystalline order in both short and long-range. This high-pressure structure shows great similarities with the structures reported in previous work [26], named Si-XIII phase.

A portion of the six-coordinated silicon atoms in region B* is shown in Fig. 7. One of the unit cell is also abstracted from the repeated

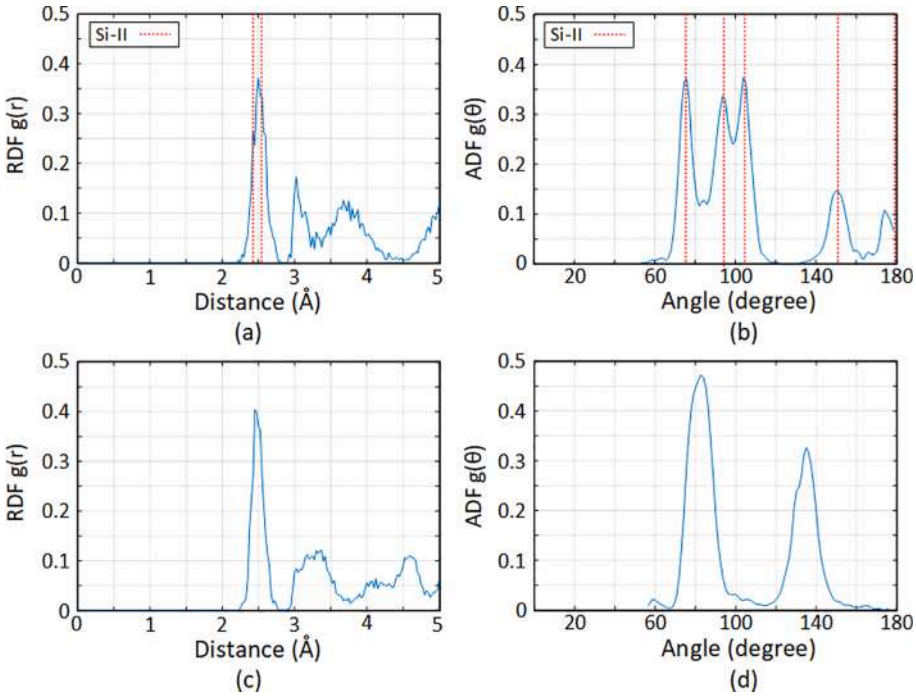

Fig. 6. RDF and ADF of the six-coordinated silicon atoms belonging to (a) and (b) Si-II, (c) and (d) Si-XIII phase.

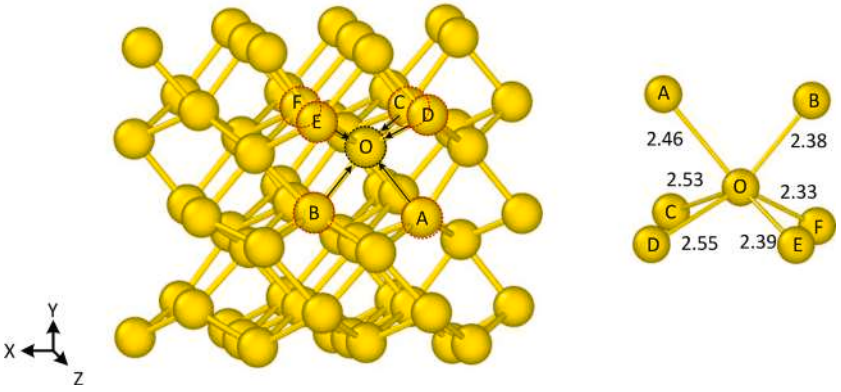

Fig. 7. (a) A portion of the atoms in region B* showing its crystalline structure. (b) Structure of one unit in region B*. The bond lengths are shown in Å.

crystalline structures with detailed bond length. It is clear that the unit cell of Si-XIII is completely different from that of Si-II, including bond length and bond angle. Therefore, this crystalline structure belongs to a new kind of six-coordinated silicon phase.

Furthermore, the six-coordinated silicon atoms on the different crystallographic surfaces are future investigated. The ADF of the six-coordinated atoms are calculated as shown in Fig. 8. It is found that the trends on (001), (101), and (111) oriented surfaces present different characteristics. Although these six-coordinated silicon atoms present a compounded characteristic of several crystalline structures and amorphous phase, some features can be extracted from the statistical result. For the (001) and (101) oriented surface, the two sharp peaks at 87° and 135° are corresponding to the bond angle of the Si-XIII phase. Compared with (001) oriented surface, all the ADF peaks widely broadened for (111) oriented surface, the evidence of the existence of Si-XIII being in the six-coordinated silicon atoms is inadequate.

To further ensure the phase transformation process in the nanoindentation process, the variation of coordination number of silicon atoms versus time steps is shown in Fig. 9. The indenter is kept unchanged for at least 10,000 steps at the maximum depth. By determining the CN of these silicon atoms, it is found that there is a transition process after rapid loading. The number of six- and seven-coordinated silicon atoms remains stable in that period of holding time for the (001), (101) and (111) oriented surface. While for the five-coordinated silicon atoms, the total number of such atoms is till increasing even when the indenter is remained unchanged, especially for the (101) oriented surface. This also indicates that the five-coordinated atoms maybe act as an intermediate unstable phase and shows hysteresis effect in the loading process. While in the unloading process, these silicon atoms lose their compact structures. This means that these obtained high-pressure phases is stable as long as the surrounding stress is maintained.

Another interesting phenomenon is the ratios of different coordinated silicon atoms on different crystallographic surfaces, especially for five- and six-coordinated atoms. In the case of nanoindentation on Si (101) oriented surface, the largest amount of five-coordinated silicon

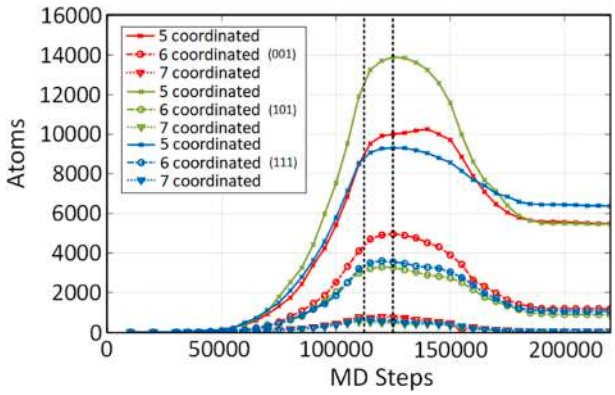

Fig. 9. Number of atoms with specified nearest number of neighbors versus time steps. After the first loading stage for 100,000 time steps, the indenter is deliberately held at the maximum indentation depth for 10,000 time steps.

atoms appears with the lowest amount of six-coordinated silicon atoms. For the cases on (001) and (111) oriented surfaces, the ratios between the five- and six-coordinates silicon atoms are lower than that on the Si (101) oriented surface. In another word, if the five-coordinated silicon atoms are regarded as an intermediate/transition phase for six-coordinated Si-II phase, the five-coordinated silicon atoms on (001) oriented surface have larger possibility to complete the phase transformation to other high-pressure metastable phase.

3.2. Phase transformation during nanoindentation on (001)

As stated above, on the (001) oriented surface, two kinds of six-coordinated high-pressure phases, Si-II and Si-XIII, are formed beneath the indenter during the nanoindentation. One high-pressure phase Si-II distribution under large indentation load has been widely reported on different silicon crystallographic surfaces. The other high-pressure

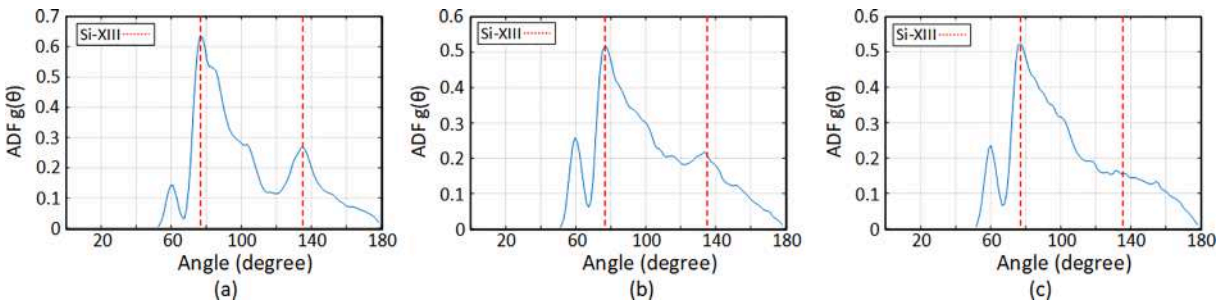

Fig. 8. ADF of six-coordinated silicon atoms on the crystallographic surfaces (a) (001) (b) (101), and (c) (111) oriented surfaces.

phase Si-XIII is seldomly reemerged and investigated by simulations or experiments, and thus we are short of clear understanding on its evolution under pressure.

To understand the phase transformation process of these six-coordinated silicon atoms, the atomic behavior at different depths from the contact surface should be tracked, as shown in Fig. 10. Two groups of atoms are monitored in the whole loading and unloading process, marked with A* and B* in the subsurface. As the indenter presses into the (001) oriented surface, the pristine diamond cubic structure begins to transform into other phase structures and the deformed area becomes large, as the dashed line T_1-T_1 in Fig. 10(c) and (d). These two groups of six-coordinated silicon atoms are also involved in the deformed region, while belongs to different high-pressure crystalline structures. When the indenter retracts from the maximum depth, these two crystalline structures present different behaviors. The red cross-mark in Fig. 10(c) indicates the largest depth of the transformation region and keeps constant in the following the steps in Fig. 10(d)–(f). From Fig. 10(d)–(f), the atoms region A* is transformed into amorphous atoms and there is no visible change of the outline of the deformed region except the elastic recovery of the bulk material after unloading. However, for the region B*, the atomic behavior, with similar deformation expansion on loading, is totally different upon unloading process. The outline of transformed region, T_1–T_1 to T_4–T_4, changes dramatically, from convex to concave. It means the phase transformation for Si-II-to-amorphous is discriminate from the transformation for Si-XIII upon retraction.

For further understanding the phase transformation for these two six-coordinated phases, the local atomic structures are extracted from the loading to the unloading processes as shown in Figs. 11 and 12. The red atoms in the structure are selected to be monitored during the whole process. The other atoms are classified by CN and in different colors. For both of the evolutions, the processes are divided into 8 steps, among 5 of which are in the loading process. For the Si-I to Si-II phase transformation (Fig. 11 1–5), seven silicon atoms in pristine diamond cubic structure are located in three neighbor unit cells as shown in Fig. 11 1. As the indenter presses into the bulk silicon, the silicon atoms that close to the indenter are firstly impressed and the coordination increases from four to six, while several layers of five-coordinated atoms, as a transition region, are generated between these two regions with four- and six-coordinated atoms, respectively. With the further pressing of the indenter, the six-coordinated atoms go further towards the four-coordinated pristine diamond cubic silicon atoms and the coordination of marked red silicon atoms changes from four to six. The crystalline structure of the Si-II is fully taken into shape when the six-coordinated atoms cover the whole marked red silicon atoms. However, when the indenter retracts from the maximum depth, the high-pressure Si-II phase atoms fail to recover to their pristine diamond cubic structure. One part of the silicon atoms transforms into amorphous phase, while the rest of the Si-II and bct5 atoms still maintain in the deformed region. The amorphous atoms are in disorder and randomly distributed without long-range order. As the surrounding stress releases, the local density of the amorphous atoms decreases and most of the coordination converges at five and four.

For the evolution process of Si-XIII phase in the nanoindentation, it presents some similarities with phase transformation of Si-II in loading stated above. For instance, the initial silicon atoms are also located in the three neighbor unit cells and the marked silicon atoms also encounter a five-coordinated transition region. Contrast to the Si-II phase transformation in unloading process, the behavior of Si-XIII atoms is different, as shown in Fig. 12 7. In the extracted local structures, some part of the Si-XIII atoms recovers to the pristine diamond cubic silicon atoms and the rest, like the Si-II phase transformation in

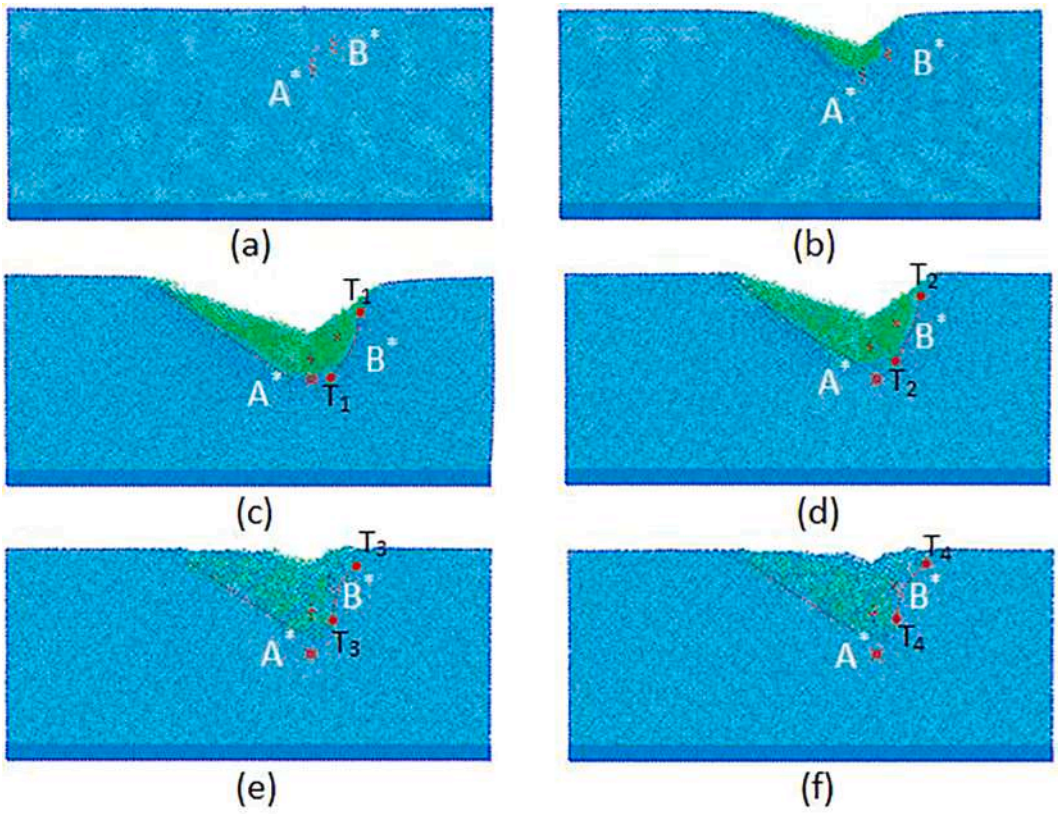

Fig. 10. Snapshots of atom positions at different loading/unloading stages. Silicon atoms are colored to distinguish the deformed and pristine region. The blue and green ones are pristine diamond silicon atoms and deformed atoms. (a) At the indentation depth of 0 nm, (b) 2.0 nm, (c) 4.0 nm, (d) 3.0 nm, (e) 1.0 nm, (f) 0 nm. (For interpretation of the references to colour in this figure legend, the reader is referred to the web version of this article.)

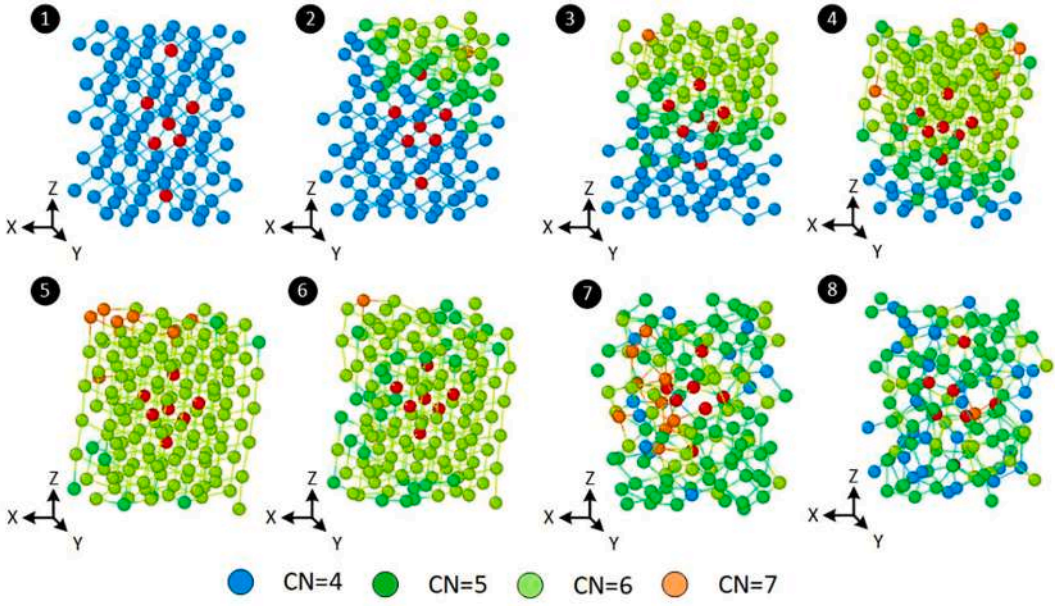

Fig. 11. Si-II evolution in loading and unloading. The targeted atoms are from the region A* in Fig. 10. Steps 1 to 5 belong to the loading phase, while the rest belongs to extraction phase.

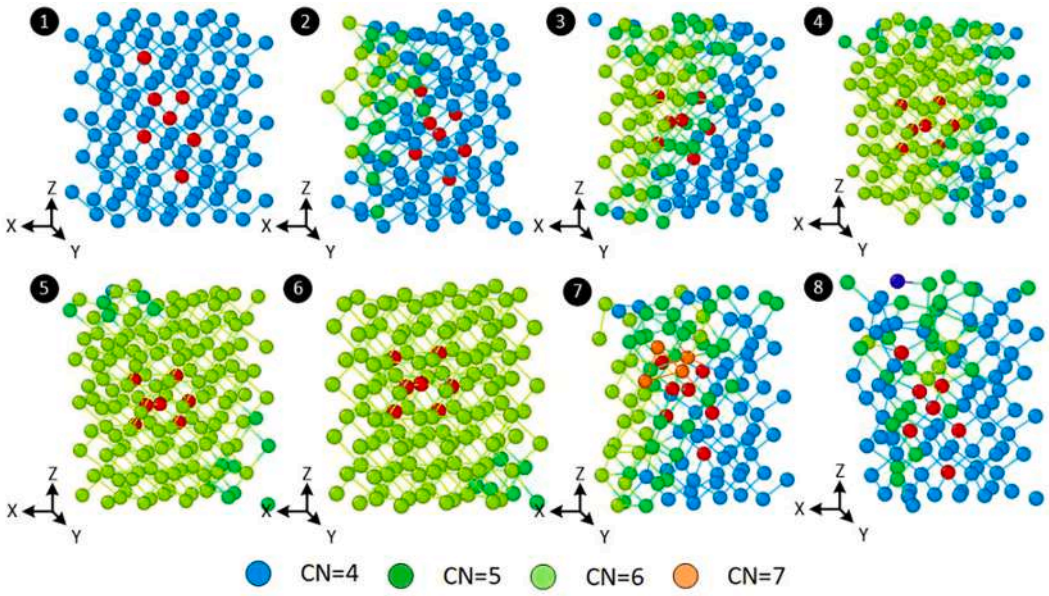

Fig. 12. Si-XIII evolution in loading and unloading. The targeted atoms are from the region B* in Fig. 10. Steps 1 to 5 belong to the loading phase, while the rest belongs to extraction phase.

unloading process, transforms into amorphous atoms.

3.3. Hydrostatic and von mises stress

It is generally accepted that it is the flattening the diamond cubic structure that causes the phase transition from Si-I to Si-II. The loading should be along the (0 0 1) oriented crystalline direction and the transition is triggered by the hydrostatic pressure beneath the indenter. It is also accepted that the introduction of shear stress or deviation stress, which are generally generated in the nanoindentation, can promote the phase transition process [36]. Neither of the hydrostatic pressure, nor the von Mises stress or the deviation stress can individually evaluate such process under complex stress conditions.

To deeply explore the effects of these stresses, atomic stresses is obtained by the virial theorem. The average value of the stress in local spherical region (~5 A) is calculated as Ref. [1]. Fig. 13 presents the cross-section views of the hydrostatic pressure and the von Mises stress at the maximum depth on the (0 0 1) oriented surface. Some similarities of the hydrostatic pressure and von Mises stress are illustrated in Fig. 13. For example, the stresses are concentrated to the edges of the indenter and shows nonuniformity on stress distribution at different regions beneath the indenter. The largest hydrostatic pressure is 21.8 GPa, and the largest von Mises stress is over 27.8 GPa. The two regions of the six-coordinated crystalline structures are surrounded with dashed line A* and B*. It is noted that the hydrostatic pressure for these two regions are both above 12 GPa at the maximum depth. Compared with the region B*, the region A* suffers with severe shear stress. But with the maximum von Mises stress region, only amorphous silicon atoms are found. On the

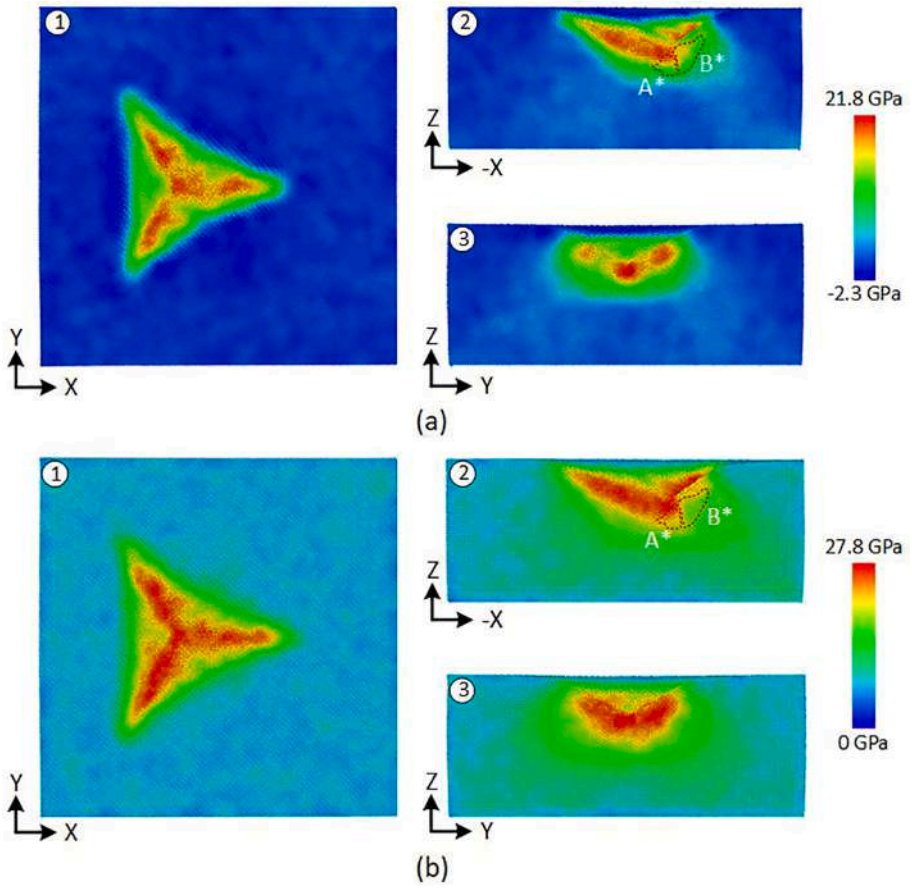

Fig. 13. Views of hydrostatic pressure and von Mises stress contour at the maximum nanoindentation depth. The regions A* and B* marked with dash line in the subgraph are from Fig. 2 (a), correspond to two six-coordinated high-pressure Si-II and Si-XIII phases.

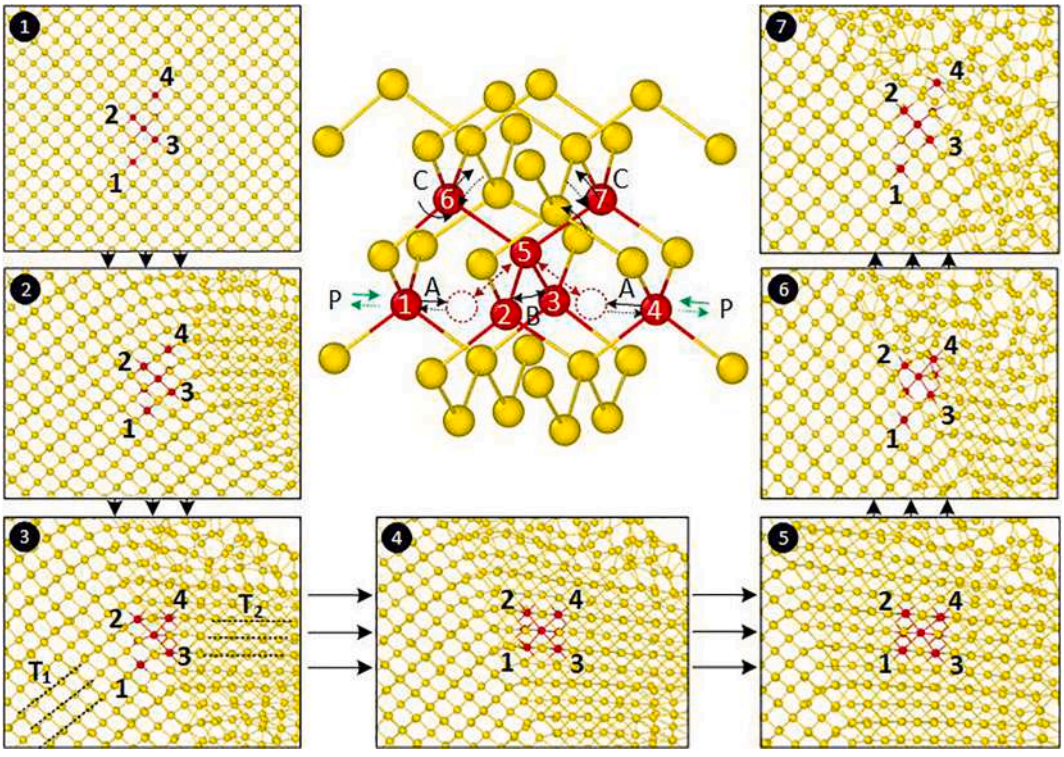

Fig. 14. The evolution of crystalline structure from Si-I to Si-XIII by tracking atomic positions in the whole nanoindentation process.

face of it, this result implies the different von Misses stress should be responsible for the different phase transformation from Si-I to Si-II and Si-XIII. The phase transformation is not consistence with either of the hydrostatic pressure or the von Mises stress in the nanoindentation. Hence, both of the hydrostatic pressure and von Mises should be considered in the phase transformation.

4. Discussion

The present research indicates that the phase transformation of six-coordinated phases on (0 0 1) is quite different with that on (1 1 0) and (1 1 1) oriented surfaces. On the (0 0 1) oriented surface, two different crystalline structures of six-coordinated silicon phases are discovered. Both of them are located at different regions beneath the indenter. From previous research, it is clear that the phase transition from Si-I to Si-II, which is accomplished with the flattening of the diamond cubic structure with [0 0 1] oriented direction compression over 12 GPa [23]. The atoms in three neighboring unit cells transform into Si-II phase, as the illustration in Fig. 11. However, from the simulation result above, the formation of Si-XIII has some similarities with Si-II.

The phase transformation from Si-I to Si-XIII are shown in Fig. 14. As shown in the atomic structure transition, in the pristine diamond cubic Si-I structures, the silicon atoms #2, #3, #6, #7 are on the vertices of a tetrahedron with a central atom #5, with a bond length of 2.35 Å and bond angle of 109.5°. The subgraph 1 presents the pristine positions of the silicon atoms before nanoindentation. When the compression pressure was applied on the structure, the positions of several atoms in/near the pristine diamond cubic structure begin to change with the bending of the crystallographic plane, involving bond length and bond angle. As illustrated in subgraph 3, when the crystallographic plane (T_1–T_2) is bended ~45° around the [0 1 0] axis, one of the atoms (#4) near the pristine lattice structure is driven towards the central atom (#5) with a small rotation. At the same time, the silicon atom (#7) moves to the centerline of the atoms #3 and #4, and due to the strong repulsive force between these atoms, the bond angles of atoms (#4–#5–#7 and #3–#5–#7) become larger. With larger area is deformed by compression pressure (subgraph 4 and 5), the atoms marked with red color are completely transformed into Si-XIII crystalline structure, the bond angles (#2–#5–#3) being flatten, and silicon atom (#1, #6) symmetrical to the atom (#4, #7), respectively. In short, three remarkable movements of the atoms in the lattice structure are illustrated and marked with A, B and C. In order to compromise the local compression pressure and deformation, the silicon atoms in pristine diamond cubic structure rotate (C) along two directions [0 1 0] and [0 0 1]. The silicon atoms near to the pristine diamond cubic structure move (A) close to the central atom as the bending deformation of the crystallographic plane. Finally, the silicon atom in the pristine diamond cubic lattice is flattened (B).

On the contrary, the behavior of the high-pressure silicon phase Si-II is different from the phase transformation of Si-XIII after stress releasing. In the subgraph (6 and 7), when the stress is releasing, part of the Si-XIII phase transforms into amorphous atoms, which is close to the indenter, while the others recover back to the pristine diamond cubic structure with the recovery of the bended crystallographic plane.

Combined with the hydrostatic pressure and von Mises stress contour beneath the indenter, it is clear that the von Mises stress inside the region of Si-II phase is much larger than that in the region of Si-XIII phase with similar hydrostatic pressure. It shows that these two different high-pressure silicon phases are generated with different local shear stress. The local elastic deformation of certain crystalline surfaces promotes the phase transformation from Si-I to Si-XIII inside the region. The Si-XIII phase is also generated in the case on (1 0 1) oriented surface and the Si-I to Si-XIII phase transformation encounters in the similar way as described on the (0 0 1) oriented surface. Hence, the phase transformation Si-II to Si-XIII can be regarded as a general transition process on the monocrystalline silicon nanoindentation.

5. Conclusions

Large-scale molecular dynamics simulations are conducted to investigate the phase transformation on silicon surfaces (0 0 1), (1 0 1), and (1 1 1) by nanoindentation using a Berkovich indenter. Different from the spherical indenter, some interesting phenomena occur in the nanoindentation with Berkovich indenter. The types and distribution of the high-pressure silicon phases are different depending on crystallographic surfaces. For the bct5 and DDS extend along different crystallographic directions and generate various symmetrical patterns. It is also noted that the distributions of the bct5 is consistent with the {1 1 1} [1 1 0] slip systems, while DDS encounters elastic deformation by pressure occurred in the loading process and recovers to pristine diamond cubic silicon after pressure releasing.

An amount of high-pressure six-coordinated phase Si-XIII is discovered on (0 0 1) oriented silicon surface. The Si-II and Si-XIII phases coexist beneath the indenter but in different regions. The evolution of these two high-pressure phases from pristine diamond cubic silicon phase Si-I are carefully investigated by tracking atomic positions in the loading process. Although the bct5 phase is presented in both phase transformations, the silicon atoms undergo different transitions. The completeness of Si-XIII phase transformation is accompanied with elastic deformation of crystalline surfaces, while the Si-II are achieved by irreversible transition and deformation. We also discovered that, upon complete unloading, part of the Si-XIII atoms transforms into amorphous atoms while the others recover to Si-I. Finally, the local hydrostatic pressure and von Mises stress are obtained to predict their phase transformation. The concentrated hydrostatic pressure and specific stress orientation introducing this high-pressure silicon phase. This research contributes to deepening the cognition of high-pressure silicon phase transformation and offer insight into potential links between the Si-XIII phase and the other related phases.

CRediT authorship contribution statement

Lin Zhang: Conceptualization, Methodology, Software, Writing - original draft. **Jiwang Yan:** Writing - review & editing, Supervision, Project administration.

Declaration of Competing Interest

The authors declare that they have no known competing financial interests or personal relationships that could have appeared to influence the work reported in this paper.

Acknowledgment

Lin Zhang is an International Research Fellow of the Japan Society for the Promotion of Science (JSPS). This study has been financially supported by Grant-in-Aid for JSPS Fellows (Grant No. P20368).

References:

[1] J. Sun, L. Fang, J. Han, Y. Han, H. Chen, K. Sun, Phase transformations of monocrystal silicon induced by two-body and three-body abrasion in nanoscale, Comput. Mater. Sci. 82 (2014) 140–150.
[2] H.u. Huang, J. Yan, New insights into phase transformations in single crystal silicon by controlled cyclic nanoindentation, Scr. Mater. 102 (2015) 35–38.
[3] H.u. Huang, J. Yan, On the mechanism of secondary pop-out in cyclic nanoindentation of single-crystal silicon, J. Mater. Res. 30 (11) (2015) 1861–1868.
[4] J. Yan, H. Takahashi, J. Tamaki, X. Gai, H. Harada, J. Patten, Nanoindentation tests on diamond-machined silicon wafers, Appl. Phys. Lett. 86 (18) (2005) 181913, https://doi.org/10.1063/1.1924895.
[5] S.W. Youn, C.G. Kang, Maskless pattern fabrication on Si(100) surface by using nanoindenter with KOH wet etching, Scr. Mater. 50 (1) (2004) 105–109.
[6] S. Ruffell, J.E. Bradby, N. Fujisawa, J.S. Williams, Identification of nanoindentation-induced phase changes in silicon by in situ electrical characterization, J. Appl. Phys. 101 (8) (2007) 083531, https://doi.org/10.1063/1.2724803.

[7] J.S. Williams, M.V. Swain, J.E. Bradby, In situ electrical characterization of phase transformations in Si during indentation, Phys. Rev. B 67 (8) (2003), 085205.
[8] J. Crain, G.J. Ackland, J.R. Maclean, R.O. Piltz, P.D. Hatton, G.S. Pawley, Reversible pressure-induced structural transitions between metastable phases of silicon, Phys. Rev. B 50 (17) (1994) 13043–13046.
[9] R.O. Piltz, J.R. Maclean, S.J. Clark, G.J. Ackland, P.D. Hatton, J. Crain, Structure and properties of silicon XII: a complex tetrahedrally bonded phase, Phys. Rev. B 52 (6) (1995) 4072–4085.
[10] I. Zarudi, L.C. Zhang, J. Zou, T. Vodenitcharova, The R8–BC8 phases and crystal growth in monocrystalline silicon under microindentation with a spherical indenter, J. Mater. Res. 19 (1) (2004) 332–337.
[11] Z. Zeng, Q. Zeng, W.L. Mao, S. Qu, Phase transitions in metastable phases of silicon, J. Appl. Phys. 115 (10) (2014) 103514, https://doi.org/10.1063/1.4868156.
[12] H. Huang, J. Yan, Volumetric and timescale analysis of phase transformation in single-crystal silicon during nanoindentation, Appl. Phys. A 122 (6) (2016) 607.
[13] L. Chang, L.C. Zhang, Deformation mechanisms at pop-out in monocrystalline silicon under nanoindentation, Acta Mater. 57 (7) (2009) 2148–2153.
[14] Y.B. Gerbig, S.J. Stranick, D.J. Morris, M.D. Vaudin, R.F. Cook, Effect of crystallographic orientation on phase transformations during indentation of silicon, J. Mater. Res. 24 (3) (2009) 1172–1183.
[15] T. Juliano, Y. Gogotsi, V. Domnich, Effect of indentation unloading conditions on phase transformation induced events in silicon, J. Mater. Res. 18 (5) (2003) 1192–1201.
[16] T. Juliano, V. Domnich, Y. Gogotsi, Examining pressure-induced phase transformations in silicon by spherical indentation and Raman spectroscopy: a statistical study, J. Mater. Res. 19 (10) (2004) 3099–3108.
[17] X. Du, H. Zhao, L. Zhang, Y. Yang, H. Xu, H. Fu, L. Li, Molecular dynamics investigations of mechanical behaviours in monocrystalline silicon due to nanoindentation at cryogenic temperatures and room temperature, Sci. Rep. 5 (1) (2015), https://doi.org/10.1038/srep16275.
[18] H. Zhao, C. Shi, P. Zhang, L. Zhang, H.u. Huang, J. Yan, Research on the effects of machining-induced subsurface damages on mono-crystalline silicon via molecular dynamics simulation, Appl. Surf. Sci. 259 (2012) 66–71.
[19] L. Zhang, et al., A study on phase transformation of monocrystalline silicon due to ultra-precision polishing by molecular dynamics simulation, AIP Adv. 2 (4) (2012) 042116, https://doi.org/10.1063/1.4763462.
[20] L. Zhang, H. Zhao, Y. Yang, H.u. Huang, Z. Ma, M. Shao, Evaluation of repeated single-point diamond turning on the deformation behavior of monocrystalline silicon via molecular dynamic simulations, Appl. Phys. A 116 (1) (2014) 141–150.
[21] J.J. Gilman, Shear-induced metallization, Philos. Mag. B 67 (2) (1993) 207–214.
[22] S. Jun, Y. Lee, S.Y. Kim, S. Im, Large-scale molecular dynamics simulations of Al (111) nanoscratching, Nanotechnology 15 (9) (2004) 1169–1174.
[23] W.C.D. Cheong, L.C. Zhang, Molecular dynamics simulation of phase transformations in silicon monocrystals due to nano-indentation, Nanotechnology 11 (3) (2000) 173–180.
[24] D.E. Kim, S.I. Oh, Atomistic simulation of structural phase transformations in monocrystalline silicon induced by nanoindentation, Nanotechnology 17 (9) (2006) 2259–2265.
[25] J. Sun, A. Ma, J. Jiang, J. Han, Y. Han, Orientation-dependent mechanical behavior and phase transformation of mono-crystalline silicon, J. Appl. Phys. 119 (9) (2016) 095904, https://doi.org/10.1063/1.4942933.
[26] K. Mylvaganam, L.C. Zhang, P. Eyben, J. Mody, W. Vandervorst, Evolution of metastable phases in silicon during nanoindentation: mechanism analysis and experimental verification, Nanotechnology 20 (30) (2009) 305705, https://doi.org/10.1088/0957-4484/20/30/305705.
[27] L. Zhang, H.u. Huang, H. Zhao, Z. Ma, Y. Yang, X. Hu, The evolution of machining-induced surface of single-crystal FCC copper via nanoindentation, Nanoscale Res. Lett. 8 (1) (2013) 211, https://doi.org/10.1186/1556-276X-8-211.
[28] L. Zhang, H. Zhao, L.u. Dai, Y. Yang, X. Du, P. Tang, L.i. Zhang, Molecular dynamics simulation of deformation accumulation in repeated nanometric cutting on single-crystal copper, RSC Adv. 5 (17) (2015) 12678–12685.
[29] J. Tersoff, Modeling solid-state chemistry: Interatomic potentials for multicomponent systems, Phys. Rev. B 39 (8) (1989) 5566–5568.
[30] S. Plimpton, Fast Parallel Algorithms for Short-range Molecular Dynamics, Sandia National Labs, Albuquerque, NM (United States), 1993.
[31] A. Stukowski, Visualization and analysis of atomistic simulation data with OVITO–the Open Visualization Tool, Modell. Simul. Mater. Sci. Eng. 18 (1) (2009), 015012.
[32] W. Humphrey, A. Dalke, K. Schulten, VMD: Visual molecular dynamics, J. Mol. Graph. 14 (1) (1996) 33–38.
[33] S.J. Clark, et al., Theoretical study of high-density phases of covalent semiconductors. I. Ab initio treatment, Phys. Rev. B 49 (8) (1994) 5329–5340.
[34] D.E. Kim, S.I. Oh, Deformation pathway to high-pressure phases of silicon during nanoindentation, J. Appl. Phys. 104 (1) (2008), 013502.
[35] T. Halicioglu, W.A. Tiller, H. Balamane, Comparative study of silicon empirical interatomic potentials, Phys. Rev. B 46 (4) (1992) 2250–2279.
[36] L. Zhang, et al., A study on size effect of indenter in nanoindentation via molecular dynamics simulation, Key Eng. Mater. 562–565 (2013) 802–808.